A Communication Theoretical Modeling of Single-Layer Graphene Photodetectors and Efficient Multireceiver Diversity Combining

Burhan Gulbahar and Ozgur B. Akan, *Senior Member, IEEE*

***Abstract*—Graphene with groundbreaking properties has tremendous impact on physical sciences as 2-D atomic layer carbon sheet. Its unique electronic and photonic properties lead to applications such as transistors, graphene photodetectors (GPDs), and electronic circuit components. Metal–graphene–metal (MGM) GPDs with single- or multilayer graphene sheets are promising for future nanoscale optical communication architectures because of wide range absorption from far infrared to visible spectrum, fast carrier velocity, and advanced production techniques due to planar geometry. In this paper, signal-to-noise ratio (SNR), bit-error rate (BER), and data rate performances of nanoscale single-layer symmetric MGM photodetectors are analyzed for intensity modulation and direct detection (IM/DD) modulation. Shot and thermal noise limited (NL) performances are analyzed emphasizing graphene layer width dependence and domination of thermal NL characteristics for practical power levels. Tens of Gbit/s data rates are shown to be achievable with very low BERs for single-receiver (SR) GPDs. Furthermore, multireceiver (MR) GPDs and parallel line-scan (PLS) network topology are defined improving the efficiency of symmetric GPDs. SNR performance of SR PLS channels are both improved and homogenized with MR devices having the same total graphene area by optimizing their positions with max–min solutions and using maximal ratio and equal gain diversity combining techniques.**

***Index Terms*—Diversity combining, graphene, optical network, parallel line-scan (PLS), photodetector.**

I. Introduction

GRAPHENE being a 2-D single-atomic-layer carbon atoms in a hexagonal honeycomb lattice has tremendous impact on physical sciences due to its significant and unique electronic, photonic and mechanical properties [1], [2]. It has high electron mobility and carrier Fermi velocity (1/300 of the speed of light), strong and fast broadband absorption from far infrared to visible and ultraviolet spectrum due to linear dispersion of Dirac electrons [3]–[6]. Furthermore, absorption range is tunable with external gates, by bandgap engineering forming narrow nanoribbons or applying strain and electric fields. Moreover, absorption from multiple graphene layers is additive. Combining its tremendous near-ballistic electronic transport and photonic properties with mechanical stability leads to devices operating at room temperature in nanoscale electronics and optoelectronics [3].

Graphene is similar to carbon nanotube in terms of electronic transport properties; however, it is 2-D, zero band gap and more easily produced by using advanced techniques due to its planar geometry leading to a competitive nanoscale material [7]. Graphene photodetectors (GPD) combine the wide range of optical absorption and fast carrier transport properties of graphene compared with conventional semiconductors. Recent metal–graphene–metal (MGM) experiments show strong photocurrent response reaching internal quantum efficiency of 30% and hundreds of Gbit/s data rate performance [2], [8], [9] due to photothermoelectric effect or built-in field of Schottky barriers at metal–graphene interfaces [9]–[15]. Furthermore, graphene phototransistors with p-i-n junctions show significant theoretical performance of optical responsivity, i.e., $\mathcal{R}$, and dark current detectivity [16]–[18]. Thus, ultrawideband response range and fast carrier response make GPDs potential candidates for future nanoscale optical networks.

Graphene with remarkable fast response in wide spectrum range suffers from low efficiency due to the low light–graphene interaction region, low absorption and the necessity to form multiple p-n junctions to sweep the charge carriers [2], [9], [19]. The efficiency is improved with the increased absorption of multilayer (ML) graphene [16], increased electric field region and intensity sweeping the charge carriers with multiple finger devices and asymmetric metals [9] or amplified optical fields of adaptive resonance frequencies with plasmonic nanostructures placed near the contacts [19]. However, the improvement of efficiency by diversity combining multiple receivers with optimized geometrical placement of the same total area of single layer graphene is not considered in any of these articles.

Although GPDs are experimentally and theoretically analyzed in terms of photocurrent, dark current, and cutoff bit rates, i.e., R_b, and graphene phototransistors are theoretically analyzed in terms of dark current detectivity, single-layer MGM photodetectors are not analyzed and modeled as nanoscale optical receivers in terms of fundamental performance metrics, i.e., signal-to-noise ratio (SNR), bit-error rate (BER), and R_b. In this paper, for the first time, nanoscale single-layer symmetric MGM photodetectors are analyzed in terms of performance metrics for intensity modulation and direct detection (IM/DD)

Manuscript received August 14, 2011; accepted January 27, 2012. Date of publication February 6, 2012; date of current version May 9, 2012. This work was supported in part by the Turkish Scientific and Technical Research Council (TUBITAK) under Grant #109E257, by the Turkish National Academy of Sciences Distinguished Young Scientist Award Program (TUBA-GEBIP), and by IBM through IBM Faculty Award. The review of this paper was arranged by Associate Editor M. P. Anantram.

The authors are with the Next-Generation and Wireless Communications Laboratory (NWCL), Department of Electrical and Electronics Engineering, Koc University, Istanbul 34450, Turkey (e-mail: bgulbahar@ku.edu.tr; akan@ku.edu.tr).

Digital Object Identifier 10.1109/TNANO.2012.2187068

nonreturn-to-zero ON–OFF keying modulation showing tens of Gbit/s achievable data rates with very low BERs. Performances of shot and thermal noise limited (NL) regimes are analyzed by emphasizing the width dependence and prevalence of thermal NL regime for practical power levels. Moreover, multireceiver (MR) GPDs and parallel line-scan (PLS) optical networking transmit topology are, for the first time, introduced that increase the efficiency of the detector as a novel method. Performance of maximal ratio (MRC) and equal gain (EGC) diversity combining methods are analyzed for MR devices. Nonuniform SNR of single receiver (SR) PLS spatial channels is both homogenized and improved by using MR devices with the same total graphene area. Diversity methods and optimum receiver placement defined as max–min concave quadratic and linear optimization problems are solved with the reformulation–linearization technique (RLT).

The remainder of the paper is organized as follows. In Section II, the related work on graphene optical receivers is explored. In Section III, GPDs are theoretically modeled in terms of SNR by using equivalent circuit, photocurrent, and noise analyses. Then, in Section IV, diversity methods for MR GPDs are analyzed. In Section V, PLS optical nanonetwork topology is introduced and in Section VI, SNR performance of SR is improved with MR photodetectors by solving quadratic concave and linear optimization problems. In Section VII, the proposed models and optimization schemes are numerically simulated for practical power levels. Finally, in Section VIII, the conclusions are given.

II. Related Work

MGM photodetectors forming transistors or p-n junctions are experimentally and theoretically analyzed in detail showing remarkable performance. In [10] and [11], photocurrent response in junctions of MGM devices is analyzed considering photothermoelectric contributions without analyzing fundamental performance characteristics. Single-layer, bilayer, or ML MGM devices are analyzed theoretically and experimentally in [2], [8], [9], [12]–[15] emphasizing the collection of carriers by Schottky barriers at metal–graphene interfaces or applied external bias. In experiments, photocurrent profile is obtained by scanning the laser light along GPD devices. However, in these works, fundamental SNR, BER, and R_b performance metrics are not analyzed theoretically. Furthermore, line-scan profile is not discussed in terms of a networking topology point of view, i.e., PLS topology. Although theoretical analysis of dark current detectivity of graphene phototransistors is achieved in [16]–[18], BER and R_b analyses are not performed, thermal and shot noise are not analyzed and MR diversity combining networking concepts are not discussed.

The efficiency of the photodetectors are improved significantly with ML graphenes [16] such that comparable performances are obtained compared with quantum well and quantum dot array structures. Multiple finger asymmetric devices in [9] result in a 15-fold improvement compared with the symmetric simple device in [2]. Twenty times improvement is observed in [19] with graphene combined with plasmonic nanostructures resonant at adaptive wavelengths that opens up the possibility of creating highly efficient graphene detectors. However, MR diversity combining is not presented in any of these structures as an efficiency improvement method compared with the single detector with the same total area of graphene layer. Furthermore, communication theoretical modeling of the detectors are missing in these works.

To the best of our knowledge, this is the first work theoretically analyzing single-layer symmetric MGM photodetectors as nanoscale optical receivers in terms of BER, SNR, and R_b performances. Width dependence of performance is, for the first time, analyzed for zero-band gap single-layer graphene receivers. Furthermore, MR GPD, PLS topology and diversity combining schemes are, for the first time, introduced increasing the efficiency of GPDs. Nonuniform performance of SR spatial PLS channels are both improved and homogenized by maximal ratio and equal gain diversity combining techniques and optimum receiver placement defining as concave quadratic and linear optimization problems solved with the RLT.

III. Single-Layer GPD Model

In this paper, experimentally validated MGM photodetectors are used as basic nanoscale receivers. First, MGM device geometries in the literature formed with symmetric and asymmetric metals are discussed and the symmetric one is chosen as the receiver building block in this study. Second, symmetric MGM photodetectors are analyzed by using the equivalent circuit defined in the literature. Then, position-dependent photocurrent and noise sources are modeled leading to basic SNR expressions.

A. MGM Photodetectors

In this section, two common experimentally tested GPDs, i.e., symmetric and asymmetric metal types, are presented by comparing their properties.

1) Symmetric Metals: In [2], an ultrafast MGM photodetector is introduced for single-layer and ML graphene prepared by mechanical exfoliation of graphite and graphitic flakes deposited on Si surface covered with a 300-nm-thick SiO_2 with symmetric S–D contact electrodes (Ti/Pd/Au) as shown in Fig. 1(a). Graphene channels have $L = 1$–2-μm length and $W = 1$–2.5-μm width. Furthermore, in [13] and [14], photocurrent is observed in gate doped p-n and p-n-p junctions with device geometries similar to ultrafast photodetector. In these papers, photocurrent is observed near metal–graphene interfaces and p-n junctions reaching $\approx$500-nm depth from the metal to graphene. S–D contacts of the same metal result in a symmetric energy band diagram. Local absorption induces spatially changing photocurrent whereas shining the whole graphene channel leads to zero photocurrent due to reverse currents canceling each other at each side of the graphene.

2) Asymmetric Metals: On the other hand, MGM photodetectors utilizing the whole bulk graphene channel for photocurrent are formed with multiple metal fingers of different work functions, e.g., Ti/Pd, on a SiO_2/Si substrate with backgate modulation [9]. Asymmetric metals result in better electric field

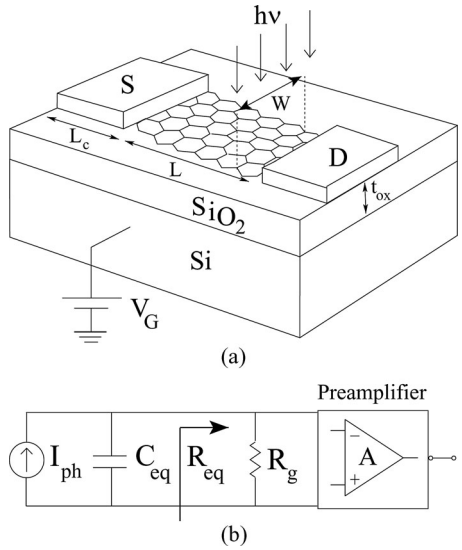

Fig. 1. (a) Device model of MGM photodetector with metallic contacts on source/drain and a modulating back gate [2], [9]. (b) Equivalent circuit for MGM photodetectors [2], [9].

modulation along graphene channel and increase photocurrent. The combined effect of multiple metal fingers and the asymmetric metals brings a 15-fold increase in [9] compared with [2]. The main photocurrent generation mechanism in both symmetric and asymmetric metal graphene detectors is the electric field that can be tuned with changing gate voltages, changing metal types and multiple fingers separated to optimize the electric field [2], [9]. Total generated photocurrent of the device is calculated by summing the local contributions obtained from each line-scan [9]. The performance of the asymmetric device compared with the symmetric device depends on the electric field improvement, number of fingers, and the absorption area that can be changed significantly with various device geometries, metal types and illuminated region. The communication theoretical comparison of the asymmetric MGM detector of various geometries with the symmetric photodetector is for the future work and is out of scope of this paper. More experimental works with asymmetric devices and their detailed theoretical modeling are necessary to formulate the asymmetric MGM device performance on each line-scan channel. However, photocurrent analysis of any GPD, whether symmetric or asymmetric, can be performed by finding the potential profile of the device along its length, then finding electric field-dependent local internal quantum efficiencies and finally summing the contributions obtained from each local line-scan. The change in the quantum efficiency, absorption constant, graphene area, and total contribution of varying number of line-scan channels for different device geometries can be easily reflected in our formulations developed in the next sections.

In this study, symmetric MGM structure with line-scan transmit power is taken as the basic receiver unit due to formation of higher resolution nanoscale spatial channels along graphene channel which is more suitable for optical nanonetwork topologies. Furthermore, asymmetric MGM devices in experiments [2], [9] are entirely illuminated to best utilize the devices. The proposed diversity combining scheme in this study creates high-resolution channels with uniform performance that are not available and desired in asymmetric MGM devices performing under entirely illuminated conditions. However, the analysis performed for symmetric metals in this paper can be easily extended to include asymmetric metal cases and various device geometries by using the experimental potential profiles of asymmetric photodetectors with the respective proportional internal quantum efficiencies. The improvements coming from higher electric fields, multiple fingers, or combining effect of multiple devices can be found based on the calculation procedure of local photocurrents in each line-scan.

Next, the basic equivalent circuit of symmetric MGM devices is discussed by using the models defined in the recent literature.

B. Equivalent Circuit Model

Photodetectors are described by equivalent circuits to compute R_b and SNR [20]. Single-layer MGM photodetectors are modeled in [2] as shown in Fig. 1(b) where photocurrent is parallel to the intrinsic resistance of graphene [2]. Single-layer graphenes having widths larger than 10–25 nm are assumed to have zero bandgap such that 2-D graphene layer forms ohmic contacts with the metals and have linear I_{ds}–V_{ds} relationship [21], [22]. The device has zero dark current with zero bias [2].

R_g denotes the graphene resistance, R_{eq} is the equivalent resistance of preamplifier and graphene combination and I_p denotes photocurrent. The total resistance of a graphene flake can be described by $R_{\mathrm{tot}} = R_{\mathrm{bulk}} + 2R_c = \rho_{\mathrm{sh}} L/W + 2\rho_c/(L_c W)$ where ρ_{sh} and ρ_{shc} denote the sheet resistances of graphene channel and the region under the contacts, respectively, L_c is the contact length, L and W are graphene channel length and width, respectively [23]. In this study, photodetectors are assumed to have same L with varying W. Therefore, $R_g = R_0(L, L_c)/W$ where $R_0(L, L_c)$ is the unit resistance per width.

Device capacitance includes the series combination of quantum, i.e., $C_Q \approx 2E_F q^2/(\pi\hbar^2 v_F^2)$ where E_F is the Fermi level and v_F is the Fermi velocity [24], and oxide capacitances, i.e., $C_{ox} = \epsilon_r \epsilon_0 / t_{ox}$ where ϵ_r is the relative permittivity of the oxide. Furthermore, parallel pad capacitances of the contacts are important in GPD experiments [2]. C_{eq} is used to find RC-limited cutoff data rate in the next sections. Next, photocurrent is modeled by extracting from experimental photocurrent profile of symmetric MGM devices and using fundamental equalities of optical absorption on incident area of graphene layer.

C. Photocurrent Model

Optical communication channels convert the input power to photocurrent where generated electron–hole (e–h) pairs are separated and collected at the external circuit [20], [25]. In this paper, IM/DD baseband channel is modeled as $I_r(t,\nu) = I_p(t,\nu) + n(t)$, where $I_r(t,\nu)$ is the receiver current at optical frequency ν, $I_p(t,\nu) = \mathcal{R}(t,\nu) P_i(t,\nu)$ is the signal carrying current, $\mathcal{R}(t,\nu)$ is the responsivity, $P_i(t,\nu)$ is incident power, and $n(t)$ is the independent white Gaussian noise [20], [25]. In

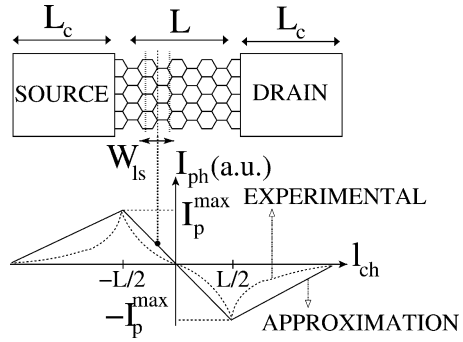

Fig. 2. Photocurrent dependence on incident optical line-scan position for MGM GPD with symmetric metal contacts for large negative V_G [13], [14].

order to compute BER, power and spatial position-dependent photocurrent is modeled with position-dependent internal quantum efficiency by extracting from the experimental photocurrent profile of symmetric MGM devices [13], [14] and using universal absorption constant of graphene [7], [27].

As shown in [14], for photodetector with length $L = 1.45\,\mu$m, at large negative gate voltages, e.g., $V_G = -40$ V, photocurrent shows maximum near contacts, decays to zero at middle and shows almost a linear behavior as shown in Fig. 2 as a result of the electric fields formed along photodetector carrying generated e–h pairs. It is approximated by linear curves without changing the overall behavior significantly based on experiments [13], [14] by concentrating on effects of line-scan position and W for constant L. Furthermore, smoother photocurrent decaying is observed in [14] which could be due to 550-nm width of line-scan incident light while in [13] 100–150-nm width leads to more nonlinear decaying. Photocurrent depends on potential gradient [13], and in [26] induced potential is shown to decay with distance x from the metal contact as $x^{-1/2}$ and x^{-1} for undoped and doped graphenes, respectively. However, more theoretical and experimental models are needed to exactly formulate photocurrent dependence in MGM photodetectors and is out of scope of this paper. Next, the efficiency metrics used in this paper are described and potential methods to increase the efficiency of the graphene-based photodetectors are discussed.

1) Efficiency of GPDs: Internal quantum efficiency is defined as $\eta_{In} \equiv |I_p| h\nu q^{-1} P_a^{-1}(\nu)$ where $P_a(\nu)$ is the absorbed power, h is Planck's constant, and q is the electric charge [20]. Then, photocurrent at line-scan position $l_{\rm ch}$ is approximated as shown in Fig. 2 as $I_p(\nu, l_{\rm ch}) = -q(P_a(\nu, l_{\rm ch})/h\nu)\eta_{In}(l_{\rm ch})\mathrm{sgn}(l_{\rm ch})$ where $\eta_{In}(l_{\rm ch}) = 2C_1|l_{\rm ch}|/L$ is internal quantum efficiency at $l_{\rm ch} \in [-0.5L, 0.5L]$, $C_1 > 0$ is a normalization constant and sgn(.) is the *sign* function. Photocurrent from contacts is due to internal photoemission and thermal injection [14], [28] and ignored to concentrate on intrinsic graphene properties.

Single-layer graphene being only one atom thick is shown to absorb $\alpha = \%2.3 = \pi/137$ of the incoming white light independent of wavelength as a result of its unique electronic structure [7], [27]. It absorbs light over a wide spectral range spanning visible and infrared ranges allowing photodetectors working in a wideband spectrum. In [9], strong photocurrent response is observed at wavelengths $0.514, 0.633, 1.55$, and $2.4\ \mu$m emphasizing the ultrawide 0.3–$6\ \mu$m range of operation. Therefore, photocurrent for incident light of width W_{ls}, i.e., $I_{ph}(\nu, l_{\rm ch})$, at incident power density $P(\nu)$ (W/m^2) is described as follows:

$$I_p(\nu, l_{\rm ch}) = \varsigma(l_{\rm ch}) \frac{\alpha P(\nu) W_{ls} W}{h\nu} \tag{1}$$

where $\varsigma(l_{\rm ch}) \equiv -2qC_1 l_{\rm ch}/L, l_{\rm ch} \le |L/2|$. Typical line-scan width, i.e., W_{ls}, ranges from 100 nm to 5 μm in GPD experiments [2], [9], [10], [13], [14], [22], [29]–[31]. Therefore, graphene channel is divided into $N_{ls} = L/W_{ls}$ spatial channels.

Although the efficiency of the single-layer symmetric detector is low, the developed communication theoretical method in this paper can be applied to other device geometries where the main mechanism is the developed electric field sweeping the generated pairs to the metal contacts with a specific internal quantum efficiency and light absorption rate.

There are different methods to increase the efficiency of the graphene detectors. Symmetric detectors give zero current under the illumination of the whole device and only a small area is effective to form the photocurrent [19]. This can be solved with multiple (asymmetric) metal fingers of different work functions [9]. Furthermore, the efficiency is improved by creating a wider photodetection with a longer light graphene interaction length with waveguides [32]. The reduction of the internal resistance is another improvement factor [2].

The low efficiency of light absorption, i.e., $\alpha = \%\,2.3$ of the incoming light, highly restricts the potential utility of the detector [2], [16], [19]. Bilayer, trilayer, or ML graphene structures absorb linearly increasing amounts of incident light, i.e., $\alpha_{\rm ML} \approx 1 - (1-\alpha)^K$ where K is the number of layers [16]. Besides that, the energy spectrum of disoriented stacks of multiple layers is the same with the single layer preserving the capabilities of single-layer detector in ML scheme too. The comparable efficiencies of ML detectors are calculated in [16] compared with quantum well and quantum dot array photodetectors.

Recently, a highly efficient, i.e., 20 times improvement compared with [2], [9], light absorption is achieved by combining graphene with plasmonic nanostructures placed near the contacts creating a field concentration at the junction regions where the generated pairs are swept [19]. The plasmonic nanostructures give the capability of the selective amplification and filtering at optical resonance frequencies depending on the geometry of the nanostructures. The contact resistances decrease and the capacitance does not change too much leading to increase in the frequency response performance. More theoretical study is necessary to analyze the dependence of the photocurrent on the combined effect of the electric field profile and the plasmonic nanostructure geometry. Next, the fundamental noise sources are computed for MGM devices and SNR is computed.

D. Noise Model and SNR

In a photodetector, three dominant types of noise are *thermal* or Nyquist–Johnson noise due to interaction of electrons with vibrating ions in resistive elements, *shot noise* due to fluctuations by the discrete nature of charge carriers [33] and 1/f noise in

the low-frequency regime, e.g., $f < 100$ kHz, for the graphene layer [34]. Since the operating frequencies reach GHz values with ultrafast GPDs, 1/f noise is neglected [2]. Shot noise is either due to photocurrent or graphene layer. For preamplifier, sources of noise other than thermal noise are neglected [33]. In [2], short circuit and $R_L = 50\text{-}\Omega$ load conditions are discussed whereas R_L is generalized to take any value in this paper. Photocurrent shot noise spectral density is described by $(\sigma_s^p)^2 = 2qI_p$ [33]. Shot noise measurement of graphene coupled to an amplifier with R_L shows that noise spectral density, i.e., $\sigma^2 = (\sigma_{\text{therm}}^{\text{eq}})^2 + (\sigma_s^g)^2$, is given as

$$\sigma^2 = \frac{4V_{T_{\text{eq}}}}{R_L} + \frac{4V_T}{R_g}\left(1 - \mathcal{F} + \mathcal{F}\frac{qIR_g}{2V_T}\coth\left(\frac{qV}{2V_T}\right)\right) \quad (2)$$

where I and V are the current and voltage across the sample, respectively, T_{eq} and T are the noise temperature of the amplifier and the bath temperature of the reservoir, respectively, $\mathcal{F}$ is the bias-dependent Fano factor [35], $V_T = \kappa T$ and $\kappa = 1.38 \times 10^{-23}$ J/K. Along this paper, it is assumed that $T_{\text{eq}} = T$. For the room temperature conditions, T is set to 300 K. At zero dark current, only thermal components are remaining, i.e., $(\sigma_s^g)^2 + (\sigma_{\text{therm}}^{\text{eq}})^2 = 4\kappa(T_{\text{eq}}/R_L + T/R_g)$ [35]. Zero dark current for symmetric MGM photodetector under zero bias is a significant property for power limited nanonetworks [2].

Derived photocurrent and noise models can be used to compute SNR of IM/DD nonreturn-to-zero ON–OFF keying modulation [20] such that information signal modulates the instantaneous transmitted optical power where photocurrent is proportional to the received power. For example, 10 Gbit/s optical link is achieved in [9] with a pseudorandom bit sequence generator modulating the light. Therefore, SNR for the ON signal is $\gamma(\nu, l_{\text{ch}}) = I_p^2(\nu, l_{\text{ch}})/(B\sigma_{\text{tot}}^2)$ where $\sigma_{\text{tot}}^2 = (\sigma_s^p)^2 + (\sigma_s^g)^2 + (\sigma_{therm}^{eq})^2$ and B is the modulating signal bandwidth. Therefore, SNRs for shot and thermal NL regions denoted by T-R_g ($R_{\text{eq}} \approx R_g$) and T-$R_L$ ($R_{\text{eq}} \approx R_L$), respectively, are given as

$$\gamma_s(\nu, l_{\text{ch}}) = \frac{(I_p(\nu, l_{\text{ch}}))^2}{2q|I_p(\nu, l_{\text{ch}})|B} = C_2'|\varsigma(l_{\text{ch}})|W \quad (3)$$

$$\gamma_{T\text{-}R}(\nu, l_{\text{ch}}) = \frac{(I_p(\nu, l_{\text{ch}}))^2}{4\kappa TB/R} = C_k'\varsigma^2(l_{\text{ch}})W^j \quad (4)$$

where $k = 3, j = 1$ for $R = R_g$ and $k = 4, j = 2$ for $R = R_L$, $C_2' = C_2 W_{ls}$, $C_3' = C_3 R_0(L, L_t) W_{ls}^2$, $C_4' = C_4 W_{ls}^2$, and the constants $C_2 = \alpha P(\nu)/(2qBh\nu)$, $C_3 = \alpha^2 P^2(\nu)/(4\kappa TBh^2\nu^2)$ and $C_4 = C_3 R_L$ are not dependent on L, W, W_{ls}, and l_{ch}. After finding width dependent SNR for SR, next, diversity combining methods are applied on a set of receivers with different graphene layer widths.

IV. Diversity Combining for MR GPD

Diversity combining methods improve SNR by combining multiple received signals [36], e.g., angle diversity for infrared optical communications [37]. Single-layer graphene experiments show position dependent photocurrent and significant loss if high responsivity metal–graphene interface regions do not get light. Moreover, low efficiency of the GPDs imposes a performance limitation and various methods such as multiple graphene layers, multiple metal fingers with asymmetric metals and plasmonic nanostructures are invented to better utilize the GPDs [9], [16], [19]. Therefore, to create more robust photodetectors performing independent of the illumination position of the line-scan and to increase the efficiency, a diversity placement of multiple photodetectors can be used. Besides that, photodetectors with varying widths can occur due to the nonperfect production mechanisms. Diversity methods best utilize these generated devices by increasing the efficiency and create a larger area device without compromising the speed since large area leads to lower R_b [2], [37].

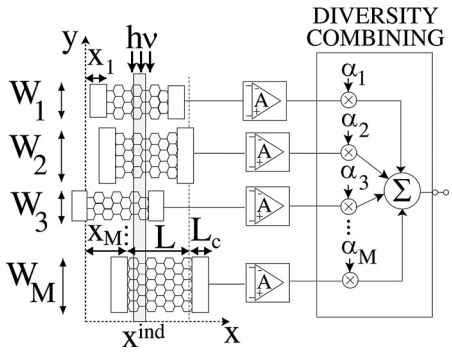

Fig. 3. Diversity combining MR GPD formed of individual GPDs with various widths and positions where line-scan optical light is incident at x^{ind}.

A MR GPD design is shown in Fig. 3 where the light is incident on $0 < x^{ind} < L$ where there are M receivers with widths W_i, same length L, x-axis coordinates x_i for $i \in [1, M]$ and the same orientation with respect to a reference coordinate system. Furthermore, photocurrent contributions from contacts are ignored to concentrate on graphene properties of wide-band absorption and fast carrier velocity.

Conventional diversity combining schemes, i.e., maximal ratio and equal gain combining, are utilized in this study. Maximal ratio combining maximizes the output SNR resulting in sum of input SNRs and equal gain combining is the solution without using the knowledge of SNRs [36]. Each branch is multiplied by $\alpha_i = r_i e^{-j\theta_i}$ where $e^{-j\theta_i}$ is the co-phasing component to constructively add the components. Here, θ_i is $\pm\pi$ since photocurrent can take negative values. Then, output SNRs for equal gain and maximal ratio combining, i.e., γ^{EC} and γ^{MC}, respectively, are given by [36]

$$\gamma_s^{EC}(\nu, x^{ind}) = \frac{\left(|\mathbf{I}_p^T|\mathbf{1}\right)^2}{2qB|\mathbf{I}_p^T|\mathbf{1}} = C_2'|\boldsymbol{\varsigma}_s^T|\mathbf{w} \quad (5)$$

$$\gamma_{T\text{-}R}^{EC}(\nu, x^{ind}) = \frac{\left(|\mathbf{I}_p^T|\mathbf{1}\right)^2}{\sum_{i=1}^{M}\frac{4\kappa TB}{R_i}} = C_k'\frac{\left(|\boldsymbol{\varsigma}_s^T|\mathbf{w}\right)^2}{Y_R} \quad (6)$$

$$\gamma_s^{MC}(\nu, x^{ind}) = \gamma_s^{EC}(\nu, x^{ind}) \quad (7)$$

$$\gamma_{T\text{-}R}^{MC}(\nu, x^{ind}) = C_k'\sum_{i=1}^{M}\varsigma_s^2(x^{ind}, x_i)W_i^j \quad (8)$$

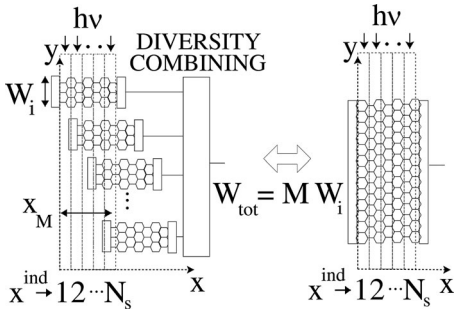

Fig. 4. Diversity combining optimization framework for spatial PLS channels by forming smaller width GPDs with sum $W_{\rm tot} = MW_i$ where the minimum SNR for channels is maximized.

where $R = R_g$ or R_L, $R_i = R_{g,i}$ or R_L, j, k are defined in (4), $Y_{R_g} = \mathbf{w}^T\mathbf{1}$, $Y_{R_L} = M$, $\mathbf{I}_p(i) = I_p(\nu, x^{ind}, x_i)$, $\varsigma_s(i) = \varsigma_s(x^{ind}, x_i)$, $\mathbf{w}(i) = W_i$, $i \in [1, M]$, $\mathbf{1}$ is the vector of ones and $\varsigma_s(x^{ind}, x_i) = \varsigma(x^{ind} - L/2 - x_i)$. Next, PLS topology is defined where diversity is utilized.

V. PLS Optical Nanonetworking

Line-scan transmitter-receiver networking topology is better suited for broadcast to cover the whole width of graphene channel in a rectangular planar receiver geometry and to create distinct and controlled spatial subchannels with high resolution. Therefore, line-scan topology can be used to broadcast the information among different devices. Although the physical mechanism to construct the topology is out of scope of this paper and in future nanoscale optical networks it can be realized, in current technology it can be realized by systems similar to a confocal Raman microscope to form the uniform intensity line illumination pattern [38]. Next, diversity combining methods are applied on SR by cutting the graphene to smaller width receivers with the same total area to create uniform spatial channels with improved SNR performance.

VI. Optimum GPD Placement and Width Selection

Symmetric MGM devices give nonuniform photocurrent, e.g., even zero response at the middle of graphene channel. Therefore, without changing length, but cutting to M parts with $W_i, i \in [1, M]$ and placing them at positions x_i can increase the minimum SNR among channels as shown in Fig. 4.

Denoting the SNR output of combining scheme at $x_p^{ind} = (p - 0.5)W_{ls}, p \in [1, N_s]$ as $\gamma_{n\rm type}^{\rm DC}(\nu, p)$ where $n$type denotes NL regimes, nonlinear optimization problem maximizing the minimum SNR among PLS channels is defined as

$$\max_{\mathbf{w},\mathbf{x}} \min_{p=1,2,\ldots,N_s} \quad \gamma_{n\rm type}^{\rm MRC,EGC}(\nu, p)$$
$$\text{s.t.} \quad \mathbf{w}^T\mathbf{1} = W_{\rm tot}, W_{\min} \le \mathbf{w} \le W_{\rm tot}, 0 \le \mathbf{x} \le L \quad (9)$$

where $\mathbf{x} = [x_1 x_2 \ldots x_M]$ and $W_{\min}$ is the minimum zero-band gap width, i.e., ≈25 nm [21], [22]. The problem complexity is reduced by separating the width and placement selection by forming M equal width receivers. Furthermore, since $|\varsigma_s(x^{ind}, x_i)|$ and $\varsigma_s^2(x^{ind}, x_i)$ are discontinuous at $x^{ind} - x_i \in \{0, 0.5L, L\}$ and $\{0, L\}$, respectively, $\mathbf{x}$ is divided into intervals to obtain continuous constraints. Hence, problem of shot NL regime is converted to the following

$$\max_{\mathbf{x}} \ u \ \text{s.t.} \ C_2' \sum_{i=1}^{M} \varsigma_s(x_p^{ind}, x_i) W_i \ge u, p \in [1, N_s] \quad (10)$$

which is a linear programming (LP) problem solved with Linear Interior Point Solver (LIPSOL) implemented under MATLAB [39]. Problem for thermal NL case is given as

$$\max_{\mathbf{x}} \ u \ \text{s.t.} \ C_k' \sum_{i=1}^{M} \varsigma_s^2(x_p^{ind}, x_i) W_i^j \ge u, p \in [1, N_s] \quad (11)$$

where $\mathbf{x}_{\min} \le \mathbf{x} \le \mathbf{x}_{\max}$, k equals to 3 and 4, j equals to 1 and 2 for T-R_g and T-R_L NL cases, respectively. The constraints can be represented as $\mathbf{x}^T\mathbf{Q_p}\mathbf{x} + \mathbf{b_p}^T\mathbf{x} + c_p + u \le 0$ where Q_p is diagonal matrix with elements h_i on diagonal. If $x_p^{ind} - L < x_i < x_p^{ind}$, $h_i = 4f_{i,j,k}$, $b_p(i) = 4f_{i,j,k}y_p$ and $c_p = -\sum_{i=1}^{M} f_{i,j,k}y_p^2$ and they are all zeros otherwise where $i \in [1, M]$, $f_{i,j,k} = -C_k'W_i^j q^2 C_1^2/L^2$ and $y_p = (L - 2x_p^{ind})$. Quadratic concave problem (negative semidefinite Q_p) can be solved by either using semidefinite programming relaxation introducing $\mathbf{X} = \mathbf{x}\mathbf{x}^T$ or LP relaxation of the RLT [40]

$$\max_{\mathbf{x}} \ u \ \text{s.t.} \ \text{Tr}(\mathbf{Q_p}\mathbf{X}) + \mathbf{b_p}^T\mathbf{x} + \mathbf{c_p} + u \le 0$$
$$\mathbf{X} - \mathbf{x}_{\min}\mathbf{x}^T - \mathbf{x}\mathbf{x}_{\min}^T + \mathbf{x}_{\min}\mathbf{x}_{\min}^T \ge 0$$
$$\mathbf{X} - \mathbf{x}_{\max}\mathbf{x}^T - \mathbf{x}\mathbf{x}_{\max}^T + \mathbf{x}_{\max}\mathbf{x}_{\max}^T \ge 0$$
$$\mathbf{X} - \mathbf{x}_{\min}\mathbf{x}^T - \mathbf{x}\mathbf{x}_{\max}^T + \mathbf{x}_{\min}\mathbf{x}_{\max}^T \le 0 \quad (12)$$

where $p \in [1, N_s]$, Tr() is the trace operator, $\mathbf{X} = \mathbf{X}^T$. Then, by dividing the interval for $0 \le \mathbf{x} \le L$ into various $\mathbf{x}_{\min} \le \mathbf{x} \le \mathbf{x}_{\max}$ where $|\varsigma_s(x^{ind}, x_i)|$ and $\varsigma_s^2(x^{ind}, x_i)$ are continuous and trying all combinations of intervals for each receiver, the maximum of the optimum solutions is chosen. Next, GPD models and optimizations are numerically simulated for practical power levels.

VII. Numerical Simulations

In this paper, η_{In} is based on experiments from [2], [8], [14] choosing the observed maximum ≈30% that can be further improved by better receiver design in future.

SR width and length are chosen as $W_{\rm tot} = 1$ μm and $L = 1.45$ μm, respectively, based on [14]. SR device is cut to $M \in [2, 40]$ receivers of $W_i = W_{\rm tot}/M$ in MR combining scheme.

The resistance measurements show variations among experiments [23], [41]. In [41], $R_c \approx (185\ \Omega{\cdot}\mu\text{m})/W$ is measured for Pd/Au contact at room temperature and for negative V_G (p-channel) emphasizing perfect contacts can decrease R_c 2 to 3 times. Thus, assuming perfect contacts, $R_c \approx (60\ \Omega{\cdot}\mu\text{m})/W$ is taken in this study. The perfection can be increased with higher mobility graphene, different metals, smaller metal–graphene coupling length, doping of graphene under metal and reduced gate oxide thickness [41]. $\rho_{\rm sh} \approx 400\ \Omega$ can be inferred from the plots in [41] for negative V_G. Therefore, $R_g = (400L + 60)/W$ where L and W are in μm.

For $0.025 < W < 1$ μm and $L = 1.45$ μm, R_g is between 0.64 and 25.6 kΩ. Even for $R_{\rm eq} \approx 25.6$ kΩ for $R_L \gg R_g$, to observe shot NL regime, i.e., $(\sigma_s^g)^2 + (\sigma_{\rm therm}^{\rm eq})^2 < 0.1(\sigma_s^p)^2$, I_p needs to be larger than 80 μA which is out of range for experiments with nA range photocurrents for practical power levels [2], [14]. Therefore, for diversity optimizations, only thermal NL regimes are analyzed. Two different R_L values are used, i.e., $R_L = 50$ Ω [2] and $R_L \geq 256$ kΩ leading to T-R_L and T-R_g NL regimes with $R_{\rm eq} \approx 50$ Ω and $R_{\rm eq} \approx R_g$, respectively.

Transmit power levels are chosen based on experiments having $\approx$50–1000 W/mm^2 densities [2], [14], [29]. Therefore, $P_{\rm in} \approx 1$ kW/mm^2 is used to find practical BER. However, BER is computed for wide range of power levels. In comparison of MR combining schemes with SR, total incident power on $0 < x^{ind} < L$ is assumed to be same for both. Since in diversity combining scheme the incident area is smaller than SR that covers whole $0 < x^{ind} < L$, incident optical power density of diversity combining schemes are increased to give the same total incident power by calculating the graphene area.

The optical wavelength is chosen as $\lambda = 1.55$ μm (193 THz) based on the experiments [2], [7], [9] that can be chosen from the ultrawideband region among wavelengths 0.3–6 μm where zero-band gap absorption of light is possible.

Line-scan positions are chosen as $\mathbf{x}^{ind} = [0.1\ \ 0.3\ \ 0.5\ \ 0.7\ \ 0.9] \times L$ where $N_s = 5$ and $W_{ls} = 0.29$ μm which is approximately average of 150–550 nm of experiments in [13] and [14]. The number of positions can be increased with higher resolution W_{ls}; however, to reduce the complexity, experimental W_{ls} resolution is good enough.

In this paper, SiO_2 of $\epsilon_r = 3.9$ and $t_{ox} = 300$ nm is used [2]. For large negative V_G and thick oxide substrates, $C_Q \gg C_{ox}$ [24] and it results in $C_g \approx C_{ox} = 0.115$ fF/μm^2. However, receiver pad capacitance is generally 2 to 3 orders of magnitude higher than graphene gate capacitance, e.g., C_p of 20–25 fF [2], which results in a parasitic capacitance limited cutoff rate [2], [42]. RC and transit time limited rates are $f_c = 1/(2\pi R_{\rm eq} C_{\rm eq})$ and $f_c = 3.5/2\pi t_{tr}$, respectively, where t_{tr} is delay of generated carriers to reach contacts. Carrier saturation velocity of 5.5×10^5 m/s leads to maximum $t_{tr} = 1.32$ ps and minimum 0.26 ps for light incident on $0.5L$ and $0.1L$, respectively [2]. The intrinsic *RC* limited rates are $f_c^{\rm min} = 1/(2\pi R_0 0.115L) \approx 1.5$ THz for T-R_g NL regime and $f_c^{\rm max} = 1/(2\pi R_L 0.115 W_{\rm min} L) \approx 760$ THz for T-R_L NL regime with $W_{\rm min} = 25$ nm. Transit time limited rates are $f_c^{\rm min} \approx 0.42$ THz and $f_c^{\rm max} \approx 2.2$ THz for $\mathbf{x}^{ind}$. Pad capacitance ($C_p = 20$ fF) RC limited rates are $\approx$310 MHz with $W = W_{\rm min}$ and $\approx$12 GHz with $W = W_{\rm tot}$ for T-R_g NL case. However, same rates are $\approx$160 GHz for T-R_L NL case for both $W_{\rm min}$ and $W_{\rm tot}$. By using C_p limited rates, maximum $\approx$12 GHz and $\approx$0.16 THz rates for T-R_g and T-R_L NL regimes, respectively, are simulated for $W = W_{\rm tot}$. Minimum rate is fixed to 100 kHz to diminish 1/f noise.

To reduce search space in (10) and (12) for large M, the optimum $\mathbf{x}$ for $M \leq 10$ is analyzed and $\mathbf{x}_{\rm opt}$ values are observed to be around the elements of $\mathbf{x}^{ind}$. Then, by averaging the optimum placements, the sets $x_i/L \in S_1 = \{0.05, 0.297, 0.497, 0.687, 0.887\}$ and $S_2 = \{0.075, 0.27, 0.483, 0.696, 0.883\}$ are constructed for shot and thermal NL cases, respectively, to be used as placement sets for larger M. Furthermore, the number of photodetectors with placements $S_{1,2}(n)$ is observed to be larger than the ones with $S_{1,2}(n+1)$ as M gets larger by further reducing the search space. Next, BER performance of SR is analyzed, and then combining methods are applied on MR GPD devices.

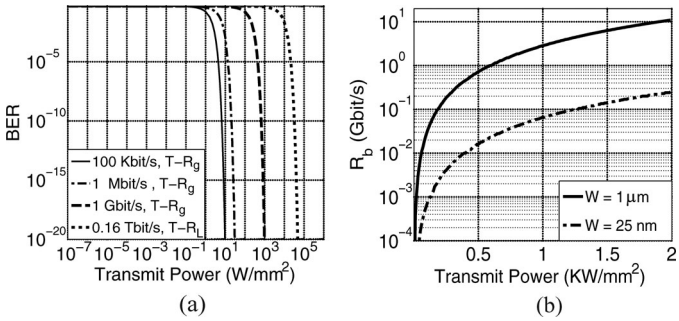

Fig. 5. (a) BER versus transmit power for varying R_b and thermal NL regions with GPD of $W_{\rm tot} = 1$ μm, (b) R_b versus practical transmit power levels for T-R_g NL region with GPDs of $W = 1$ μm and 25 nm where BER is 10^{-8}.

A. BER Performance of GPDs

BER of IM/DD nonreturn-to-zero ON–OFF keying modulation type is found with complementary error function, i.e., $\text{erfc}(x) = 2/\sqrt{\pi}\int_x^\infty e^{-x^2}dx$, with BER $= Q(\sqrt{\text{SNR}}/2)$ where $Q(x) = 0.5\,\text{erfc}(x/\sqrt{2})$ [25]. In Fig. 5(a), BER of SR for incident light on whole $0 \leq x^{ind} \leq L/2$ region is shown for T-R_g NL regime. Furthermore, for BER threshold of 10^{-8}, R_b versus transmit power is shown in Fig. 5(b) with practical power levels for both $W = W_{\rm min}$ and $W = W_{\rm tot}$. It is observed that even with very low power of $\approx$1 W/mm^2, it is possible to achieve hundreds of kilobits per second transmission with very low BER where the photocurrent generation region is $W_{\rm tot} \times L/2 = 0.725$ μm^2. It can also succeed tens of Gbit/s rate with 2-kW/mm^2 input power. Moreover, even with small area of $0.025 \times 0.775 = 0.02$ μm^2, it is possible to achieve the rate of hundreds of Mbit/s with 2-kW/mm^2 transmit power. Next, performance of MR combining methods with optimum placement are compared with SR.

B. Diversity Combining and Optimum Receiver Placement

In comparing MR diversity schemes with SR, metrics $G_{\rm MR/SR}^{\rm max,min} \equiv \text{SNR}_{\rm DC}^{\rm max,min}/\text{SNR}_S^{\rm max}$, $G_{\rm MR/SR}(x_{ind}) \equiv \text{SNR}_{\rm DC}(x_{ind})/\text{SNR}_S(x_{ind})$ and $G_{\rm MRC/EGC}$ are defined. $\text{SNR}_{\rm DC}(x_{ind})$ is the SNR obtained when x^{ind} is illuminated and its minimum $\text{SNR}_{\rm DC}^{\rm min}$, i.e., the optimized value, and $\text{SNR}_{\rm DC}^{\rm max}$ are the minimum and maximum SNR, respectively, among MR spatial channels when only the respective channel at x^{ind} receives optical signal. Similarly, $\text{SNR}_S(x_{ind})$ is the SNR for optical signal at x^{ind} for the SR device and $\text{SNR}_S^{\rm max}$ is the maximum SNR observed in SR channels, i.e., at $x_1^{ind} = 0.1L$. The rate $G_{\rm MR/SR}(x_{ind})$ gives the achievable SNR gain at the respective channels that can be used to observe the improvement in efficiency at channel level. The ratio gives the infinity value

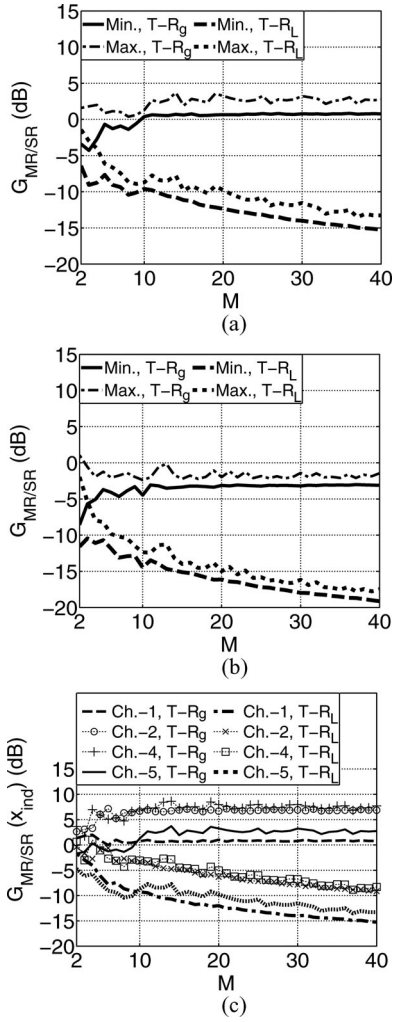

Fig. 6. $G_{\mathrm{MR/SR}}^{\max,\min}$ versus M for (a) maximal ratio combining and (b) equal gain combining, (c) $G_{\mathrm{MR/SR}}(x^{ind})$ versus M for maximal ratio combining at various channel indices, i.e., $x_k^{ind}, k=\{1,2,4,5\}$ for T-R_g and T-R_L NL cases.

at the middle channel since zero output current is obtained with the SR device. Ratio of optimized minimum values of diversity combining methods is $G_{\mathrm{MRC/EGC}} \equiv \mathrm{SNR}_{\mathrm{MRC}}^{\min}/\mathrm{SNR}_{\mathrm{EGC}}^{\min}$.

In Fig. 6(a) and (b), for T-R_g NL case, $\mathrm{SNR}^{\min}$ is increased and saturates for larger M. Maximal ratio combining in T-R_g NL regime not only creates more uniform SNRs among channels but also achieves higher SNR than the maximum SNR of SR channels, i.e., $\mathrm{SNR}_S^{\max}$. Therefore, the optimization increases the efficiency of the GPD not only by increasing SNR in the worst performance channels, e.g., zero SNR at the middle of SR, and creating a illumination position independent device performance but also increases the SNR of other channels exceeding the performance of the SR at specific line-scans. $\mathrm{SNR}_{\mathrm{MRC}}^{\min}$ reaches ≈ 0.8 dB gain and $\mathrm{SNR}_{\mathrm{MRC}}^{\max}$ reaches ≈ 3 dB gain such that the ratio between minimum and the maximum saturates. Furthermore, it is observed that the gain $G_{\mathrm{MR/SR}}(x_{ind})$ of maximal ratio combining at various channels of line-scan positions, i.e., $Ch.$-1 to $Ch.$-5 for $x_k^{ind}=(2k-1)0.1L, k\in\{1,2,4,5\}$, reaches as much as $\approx$8 dB for large M as shown in Fig. 6(c) concluding that diversity combining improves the line-scan performance of SR significantly. The performance of the channel at the middle, i.e., $Ch.$-3 of x_3^{ind}, is not plotted in Fig. 6(c) since it gives zero SNR in SR device. The optimization with respect to equal gain combining achieves to have $\mathrm{SNR}^{\min}$ and $\mathrm{SNR}^{\max}$ performances of -3 and -2 dB, respectively, at large M.

For T-RL NL regime, diversity combining performs best at minimal number of M, i.e., $M=2$. $\mathrm{SNR}_{\mathrm{MRC}}^{\min}$ and $\mathrm{SNR}_{\mathrm{EGC}}^{\min}$ gains are ≈ -6.5 and ≈ -11.5 dB, respectively, and $\mathrm{SNR}_{\mathrm{MRC}}^{\max}$ and $\mathrm{SNR}_{\mathrm{EGC}}^{\max}$ gains are ≈ -1.5 and ≈ -2 dB, respectively, such that maximum SNR channels do not degrade too much. Therefore, for T-RL NL region, uniform performance channels are obtained by sacrificing SNR in other channels. However, $\approx$0.5 and $\approx$1 dB $G_{\mathrm{MR/SR}}(x_{ind})$ gains are achieved with maximal ratio combining for $M=2$ and 4, respectively, at x_4^{ind} as shown in Fig. 6(c). Therefore, it is possible to improve SNR in some channels for T-RL NL regime in addition to obtaining homogeneous channels.

The ratio between $G_{\mathrm{MR/SR}}$ values of T-R_g and T-R_L NL regimes is M which can be calculated by using (5)–(8) and observing both schemes give same optimal placements. Due to this decreasing performance with increasing M, the degradation observed in Fig. 6(a) and (b) occurs. The increase in $\mathrm{SNR}^{\min}$ performance with increasing M for T-R_g NL case of maximal ratio combining scheme is explained as the following. From (4) and (8), it is calculated that

$$\frac{\mathrm{SNR}_{\mathrm{DC}}^{\max,\min}}{\mathrm{SNR}_S^{\max}} = \frac{P_{\mathrm{MR}}^2}{P_{\mathrm{SR}}^2}\frac{\sum_{i=1}^{M}\varsigma_s^2\left(x_{p_1,p_2}^{ind},x_i\right)}{M\varsigma_s^2\left(x_1^{ind},0\right)} \tag{13}$$

where $p_1,p_2\in[1,N_s]$ are the respective channel indices of maximal ratio combining scheme giving the maximum and minimum SNR, respectively, and P_{MR} and P_{SR} are the incident powers on MR and SR geometries, since the power density is increased for MR scheme to make the total incident power same with SR case. It is observed that the second fractional expression in (13), i.e., placement gain, is $\approx$0.23 for $M=2,3$ and then starts to oscillate around 0.35 as M increases. The power gain, i.e., $P_{\mathrm{MR}}/P_{\mathrm{SR}}$, starts from 1.38 and gradually increases with M and oscillates around 1.83 as M further increases. Therefore, SNR improvement with increasing M is the result of the combined effect of power and placement gains.

The comparison between optimum equal gain and maximal ratio combining placements of MR and SR devices is shown in Fig. 7(a). If optimization is performed independently for two schemes, maximal ratio combining gain over equal gain combining is maximum at $M=2$ with $\approx$5.2 dB, minimum at $M=3$ with 1.39 dB and saturates around 4 dB as M is increased. If maximal ratio combining optimum placement is used for equal gain combining, gain saturates around 6 dB for large M, i.e., higher than independent one since optimization is performed for maximal ratio combining. Furthermore, if equal gain combining optimum placement is used for maximal ratio combining, gain becomes much less showing that maximal ratio combining performance is not much different from equal gain combining in an optimized placement for equal gain combining.

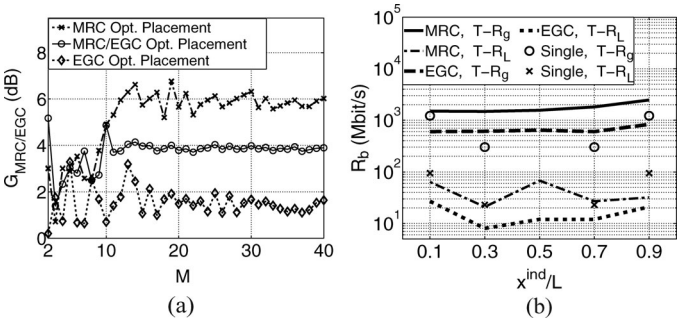

Fig. 7. (a) Maximal ratio combining versus equal gain combining for varying M showing the gain $G_{\mathrm{MRC/EGC}}$ for placements optimized with respect to maximal ratio and equal gain combining, (b) R_b versus PLS channel for SR and MR devices for BER threshold of 10^{-8} and incident power of 1 kW/mm^2.

$G_{\mathrm{MRC/EGC}}$ by using (6) and (8) can be analyzed as

$$G_{\mathrm{MRC/EGC}} = \frac{P_{\mathrm{MRC}}^2}{P_{\mathrm{EGC}}^2} \frac{M \sum_{i=1}^{M} \varsigma_s^2 \left(x_{p_1}^{ind}, x_i\right)}{\left(\sum_{i=1}^{M} \left|\varsigma_s \left(x_{p_2}^{ind}, x_i\right)\right|\right)^2} \tag{14}$$

where $p_1, p_2 \in [1, N_s]$ are channel indices having minimum SNR. The power and placement gains start from 1.15 and 2.5, respectively, at $M = 2$ to values oscillating around 1.3 and 1.4, respectively, for larger M. Therefore, power gain of maximal ratio combining increases with M, but the placement gain decreases leading to combined effect shown in Fig. 7.

The rates on channels comparing MR and SR devices are shown in Fig. 7(b) where BER is 10^{-8} and incident power for SR is 1 kW/mm^2. Even the equal gain combining scheme for T-R_g NL regime achieves almost uniform rates as much as ≈600 Mbit/s by increasing SR rates between second and fourth channels, i.e., between ≈0–300 Mbit/s. Maximal ratio combining scheme increases the corresponding rates to ≈1.5–1.8 Gbit/s showing the significant improvement and uniformity along the channel.

VIII. Conclusion

In this paper, single-layer symmetric MGM photodetectors are analyzed in terms of SNR, BER, and data rate performance metrics for IM/DD nonreturn-to-zero ON–OFF keying optical modulation by emphasizing the graphene layer width dependence. Shot and thermal NL regimes are defined observing the prevailing character of thermal NL region for practical power levels. Tens of Gbit/s data rates are shown to be achievable with very low BERs for nanoscale size GPDs. Furthermore, MR GPDs are defined combined with maximal ratio and equal gain diversity combining schemes presenting a method to increase the GPD efficiency. PLS optical networking transmit topology is introduced by emphasizing the nonuniform SNR among SR spatial channels. The homogeneity of channel performances are achieved by optimizing the geometrical placement of the defined MR devices with same total graphene area combined with diversity techniques. Maximization of the minimum SNR in spatial channels are defined as concave quadratic and linear optimization problems with an RLT solution. MR device with diversity combining techniques and optimum placement is shown to have spatial channels with more uniform and stronger SNR.

References

[1] A. Geim and K. Novoselov, "The rise of graphene," *Nat. Mater.*, vol. 6, no. 3, pp. 183–191, 2007.

[2] F. Xia, T. Mueller, Y. Lin, A. Valdes-Garcia, and P. Avouris, "Ultrafast graphene photodetector," *Nat. Nanotechnol.*, vol. 4, pp. 839–843, 2009.

[3] F. Bonaccorso, Z. Sun, T. Hasan, and A. Ferrari, "Graphene photonics and optoelectronics," *Nat. Photon.*, vol. 4, no. 9, pp. 611–622, 2010.

[4] Z. Sun, T. Hasan, F. Torrisi, D. Popa, G. Privitera, F. Wang, F. Bonaccorso, D. M. Basko, and A. C. Ferrari, "Graphene mode-locked ultrafast laser," *ACS Nano*, vol. 4, pp. 803–810, 2010.

[5] A. Wright, J. Cao, and C. Zhang, "Enhanced optical conductivity of bilayer graphene nanoribbons in the terahertz regime," *Phys. Rev. Lett.*, vol. 103, no. 20, p. 207401, 2009.

[6] J. Dawlaty, S. Shivaraman, J. Strait, P. George, M. Chandrashekhar *et al.*, "Measurement of the optical absorption spectra of epitaxial graphene from terahertz to visible," *Appl. Phys. Lett.*, vol. 93, p. 131905, 2008.

[7] P. Avouris, "Graphene: Electronic and photonic properties and devices," *Nano Lett.*, vol. 10, no. 11, pp. 4285–4294, 2010.

[8] J. Park, Y. Ahn, and C. Ruiz-Vargas, "Imaging of photocurrent generation and collection in single-layer graphene," *Nano Lett.*, vol. 9, no. 5, pp. 1742–1746, 2009.

[9] T. Mueller, F. Xia, and P. Avouris, "Graphene photodetectors for high-speed optical communications," *Nat. Photon.*, vol. 4, no. 5, pp. 297–301, 2010.

[10] X. Xu, N. Gabor, J. Alden, A. van der Zande, and P. McEuen, "Photothermoelectric effect at a graphene interface junction," *Nano Lett.*, vol. 10, no. 2, pp. 562–566, 2009.

[11] M. C. Lemme, F. Koppens, A. Falk, M. Rudner, H. Park, L. Levitov, and C. M. Marcus, "Gate-activated photoresponse in a graphene pn junction," *Nano Lett.*, vol. 11, no. 10, pp. 4134–4137, 2011.

[12] K. Lai, C. Fung, H. Chen, R. Yang, B. Song, and N. Xi, "Fabrication of graphene devices for infrared detection," in *Proc. IEEE Nanotechnol. Mater. Devices Conf.*, Oct. 2010, pp. 14–17.

[13] T. Mueller, F. Xia, M. Freitag, J. Tsang, and P. Avouris, "Role of contacts in graphene transistors: A scanning photocurrent study," *Phys. Rev. B*, vol. 79, no. 24, p. 245430, 2009.

[14] F. Xia, T. Mueller, R. Golizadeh-Mojarad, M. Freitag, Y. Lin *et al.*, "Photocurrent imaging and efficient photon detection in a graphene transistor," *Nano Lett.*, vol. 9, no. 3, pp. 1039–1044, 2009.

[15] R. Olac-vaw, H. Kang, T. Komori, T. Watanabe, H. Karasawa *et al.*, "Optoelectronic application of multi-layer epitaxial graphene on a Si substrate," in *Proc. IEEE 3rd Int. Nanoelectron. Conf.*, Jan. 2010, pp. 224–225.

[16] V. Ryzhii, M. Ryzhii, N. Ryabova, V. Mitin, and T. Otsuji, "Terahertz and infrared detectors based on graphene structures," *Infrared Phys. Technol.*, vol. 54, pp. 302–305, 2011.

[17] V. Ryzhii and M. Ryzhii, "Graphene bilayer field-effect phototransistor for terahertz and infrared detection," *Phys. Rev. B*, vol. 79, no. 24, p. 245311, 2009.

[18] V. Ryzhii, V. Mitin, M. Ryzhii, N. Ryabova, and T. Otsuji, "Device model for graphene nanoribbon phototransistor," *Appl. Phys. Expr.*, vol. 1, no. 6, p. 3002, 2008.

[19] T. J. Echtermeyer, L. Britnell, P.K. Jasnos, A. Lombardo, R. V. Gorbachev *et al.*, "Strong plasmonic enhancement of photovoltage in graphene," *Nature Commun.*, vol. 2, p. 458, 2011.

[20] J. Kahn and J. Barry, "Wireless infrared communications," *Proc. IEEE*, vol. 85, no. 2, pp. 265–298, Feb. 1997.

[21] G. Xu, C. Torres, Jr., J. Tang, J. Bai, E. Song *et al.*, "Edge effect on resistance scaling rules in graphene nanostructures," *Nano Lett.*, vol. 11, pp. 1082–1086, 2011.

[22] M. Freitag, "Optical and thermal properties of graphene field-effect transistors," *Phys. Status Solidi B*, vol. 247, pp. 2895–2903, 2010.

[23] A. Venugopal, L. Colombo, and E. Vogel, "Contact resistance in few and multilayer graphene devices," *Appl. Phys. Lett.*, vol. 96, p. 013512, 2010.

[24] T. Fang, A. Konar, H. Xing, and D. Jena, "Carrier statistics and quantum capacitance of graphene sheets and ribbons," *Appl. Phys. Lett.*, vol. 91, p. 092109, 2007.

[25] B. Gulbahar and O. B. Akan, "A communication theoretical modeling of single-walled carbon nanotube optical nanoreceivers and broadcast power allocation," *IEEE Trans. Nanotechnol.*, 2011, to be published. [Online]. doi:10.1109/TNANO.2011.2177500 [IEEE early access].

[26] P. Khomyakov, A. Starikov, G. Brocks, and P. Kelly, "Nonlinear screening of charges induced in graphene by metal contacts," *Phys. Rev. B*, vol. 82, no. 11, p. 115437, 2010.
[27] R. Nair, P. Blake, A. Grigorenko, K. Novoselov, T. Booth *et al*., "Fine structure constant defines visual transparency of graphene," *Science*, vol. 320, no. 5881, p. 1308, 2008.
[28] M. Freitag, J. Tsang, A. Bol, D. Yuan, J. Liu, and P. Avouris, "Imaging of the Schottky barriers and charge depletion in carbon nanotube transistors," *Nano Lett*., vol. 7, no. 7, pp. 2037–2042, 2007.
[29] E. Peters, E. Lee, M. Burghard, and K. Kern, "Gate dependent photocurrents at a graphene pn junction," *Appl. Phys. Lett*., vol. 97, p. 193102, 2010.
[30] E. Lee, K. Balasubramanian, R. Weitz, M. Burghard, and K. Kern, "Contact and edge effects in graphene devices," *Nat. Nanotechnol*., vol. 3, no. 8, pp. 486–490, 2008.
[31] F. Xia, T. Mueller, and P. Avouris, "Photocurrent imaging of the potential profiles in a graphene transistor," in *Proc. IEEE 21st Annu. Meet. Lasers Electro-Opt. Soc*., USA, Nov. 2008, pp. 763–764.
[32] F. Xia, J. K. Thomson, M. R. Gokhale, P. V. Studenkov, J. Wei *et al*., "An asymmetric twin-waveguide high-bandwidth photodiode using a lateral taper coupler," *IEEE Photon. Technol. Lett*., vol. 13, no. 8, pp. 845–847, Aug. 2001.
[33] S. Hranilovič, *Wireless Optical Communication Systems*. New York: Springer-Verlag, 2005.
[34] G. Liu, W. Stillman, S. Rumyantsev, Q. Shao, M. Shur, and A. Balandin, "Low-frequency electronic noise in the double-gate single-layer graphene transistors," *Appl. Phys. Lett*., vol. 95, p. 033103, 2009.
[35] R. Danneau, F. Wu, M. Craciun, S. Russo, M. Tomi *et al*., "Shot noise measurements in graphene," *Solid State Commun*., vol. 149, no. 27–28, pp. 1050–1055, 2009.
[36] A. Goldsmith, *Wireless Communications*. Cambridge, U.K.: Cambridge Univ. Press, 2005.
[37] J. Kahn, R. You, P. Djahani, A. Weisbin, B. Teik, and A. Tang, "Imaging diversity receivers for high-speed infrared wireless communication," *IEEE Commun. Mag*., vol. 36, no. 12, pp. 88–94, Dec. 1998.
[38] Fast Laser Raman Microscope: RAMAN-11. Nanophoton Corp., Osaka, Japan. (2009). [Online]. Available: www.nanophoton.jp/eng/products/raman-11/index.html
[39] Y. Zhang, "User's guide to LIPSOL: Linear programming interior point solver v0.4," *Optim. Method Softw*., vol. 11, pp. 385–396, 1999.
[40] K. Anstreicher, "Semidefinite programming versus the reformulation-linearization technique for nonconvex quadratically constrained quadratic programming," *J. Global Optim*., vol. 43, pp. 471–484, 2009.
[41] F. Xia, V. Perebeinos, Y. Lin, Y. Wu, and P. Avouris, "The origins and limits of metal-graphene junction resistance," *Nat. Nanotechnol*., vol. 6, no. 3, pp. 179–184, 2011.
[42] L. Liao, Y. Lin, M. Bao, R. Cheng, J. Bai *et al*., "High-speed graphene transistors with a self-aligned nanowire gate," *Nature*, vol. 467, no. 7313, pp. 305–308, 2010.

Burhan Gulbahar received the B.Sc. and M.Sc. degrees in electrical and electronics engineering from Bilkent University, Ankara, Turkey, in 1999 and 2002, respectively, and the Ph.D. degree in electrical and electronics engineering from Koc University, Istanbul, Turkey, in January 2012.

He had been a Research Assistant in Next-Generation and Wireless Communications Laboratory, Koc University. His current research interests include nanoscale optical communications, carbon nanotube communication networks, underwater communication networks, cognitive radio networks, wireless sensor networks, and quantum communications.

Ozgur B. Akan (M'00–SM'07) received the Ph.D. degree in electrical and computer engineering from the Broadband and Wireless Networking Laboratory, School of Electrical and Computer Engineering, Georgia Institute of Technology, Atlanta, in 2004.

He is currently an Associate Professor with the Department of Electrical and Electronics Engineering, Koc University, Istanbul, Turkey, and the Director of Next-Generation and Wireless Communications Laboratory. His current research interests include wireless communications, bioinspired communications, nanoscale and molecular communications, and network information theory.

Dr. Akan is an Associate Editor for IEEE TRANSACTIONS ON VEHICULAR TECHNOLOGY, *International Journal of Communication Systems* (Wiley), *Nano Communication Networks Journal* (Elsevier), and *European Transactions on Telecommunications*. He served as an Editor for ACM *Wireless Networks Journal* during 2004–2010, *AD HOC Networks Journal* (Elsevier) during 2004–2008, as a Guest Editor for several special issues, as the General Co-Chair for ACM The Annual International Conference on Mobile Computing and Networking, 2012, the General Chair for IEEE International Workshop on Molecular and Nanoscale Communications, 2012, the Technical Program Committee (TPC) Co-Chair for IEEE Symposium on Computers and Communications, 2012, the TPC Co-Chair for the ACM International Conference on Modeling, Analysis and Simulation of Wireless and Mobile Systems, 2010, the International Vice-Chair for IEEE International Conference on Computer Communications, 2006, and the In Organizing Committees and TPC of many conferences. He is an IEEE Communications Society Distinguished Lecturer (2011–2012), IEEE Senior Member of the Communications Society, and a member of ACM. He is the Vice-President for IEEE Communications Society—Turkey Section. He received the IEEE Communications Society Outstanding Young Researcher Award 2010 for EMEA Region (as runner-up), the IBM Shared University Research Award 2011, the IBM Faculty Award twice in 2010 and 2008, Turkish Academy of Sciences Distinguished Young Scientist Award 2008 (TUBA-GEBIP).